

Experimental verification of circular motion of Mie particles trapped within focused acoustic vortex beams

Zhengbao Li(李正宝), Hongyu Li(李洪宇), and Qingdong Wang(王青东)

Citation: Chin. Phys. B, 2025, 34 (**9**): 094303. DOI: 10.1088/1674-1056/ade857
http://cpb.iphy.ac.cn; http://iopscience.iop.org/cpb

What follows is a list of articles you may be interested in

Large-scale particle trapping by acoustic vortices with a continuously variable topological charge

Haofei Zhuang(庄昊霏), Qingyuan Zhang(张清源), Gehao Hu(胡格昊), Qingdong Wang(王青东), and Libin Du(杜立彬)
Chin. Phys. B, 2024, 33 (**7**): 074302. DOI: 10.1088/1674-1056/ad5aef

Weak-focused acoustic vortex generated by a focused ring array of planar transducers and its application in large-scale rotational object manipulation

Yuzhi Li(李禹志), Peixia Li(李培霞), Ning Ding(丁宁), Gepu Guo(郭各朴), Qingyu Ma(马青玉), Juan Tu(屠娟), and Dong Zhang(章东)
Chin. Phys. B, 2021, 30 (**4**): 044302. DOI: 10.1088/1674-1056/abca1f

Measuring orbital angular momentum of acoustic vortices based on Fraunhofer's diffraction

Chao-Fan Gong(龚超凡), Jing-Jing Li(李晶晶), Kai Guo(郭凯), Hong-Ping Zhou(周红平)†, and Zhong-Yi Guo(郭忠义)‡
Chin. Phys. B, 2020, 29 (**10**): 104301. DOI: 10.1088/1674-1056/ab9c11

Pulling force of acoustic-vortex beams on centered elastic spheres based on the annular transducer model

Yuzhi Li(李禹志), Qingdong Wang(王青东), Gepu Guo(郭各朴), Hongyan Chu(褚红燕), Qingyu Ma(马青玉), Juan Tu(屠娟), Dong Zhang(章东)
Chin. Phys. B, 2020, 29 (**5**): 054302. DOI: 10.1088/1674-1056/ab8210

Multiple off-axis acoustic vortices generated by dual coaxial vortex beams

Wen Li(李雯), Si-Jie Dai(戴思捷), Qing-Yu Ma(马青玉), Ge-Pu Guo(郭各朴), He-Ping Ding(丁鹤平)
Chin. Phys. B, 2018, 27 (**2**): 024301. DOI: 10.1088/1674-1056/27/2/024301

Experimental verification of circular motion of Mie particles trapped within focused acoustic vortex beams

Zhengbao Li(李正宝), Hongyu Li(李洪宇), and Qingdong Wang(王青东)[†]

College of Ocean Science and Engineering, Shandong University of Science and Technology, Qingdao 266590, *China*

(Received 3 May 2025; revised manuscript received 16 June 2025; accepted manuscript online 26 June 2025)

Techniques for manipulating nanodroplets lie at the core of numerous miniaturized systems in chemical and biological research endeavors. In this study, we introduce a versatile methodology for calculating the acoustic vortex field, integrating hybrid wave equation principles with ray acoustics. This approach demonstrates remarkable consistency between simulated results and experimental observations. Importantly, both theoretical analysis and experimental validation confirm that particles whose diameters match the wavelength (Mie particles) can be effectively trapped within a focused acoustic vortex field, rotating in circular trajectories centered at the vortex center. This research significantly expands the scope of acoustic vortex manipulation for larger particles and introduces a novel implementation strategy with potential applications in targeted drug delivery for clinical adjuvant therapy.

Keywords: focused acoustic vortex, ray acoustic, topological charge, circular trajectories, Mie particles

PACS: 43.72.+q, 43.38.Hz

DOI: 10.1088/1674-1056/ade857 **CSTR:** 32038.14.CPB.ade857

1. Introduction

Since optical tweezers were first proposed in 1986,[1] people have successfully applied optical tweezers to the field of particle manipulation.[2] Optical tweezers are used to manipulate smaller microparticles, and optical waves have difficulty penetrating opaque media. Compared with optical waves, acoustic waves can manipulate larger particles and penetrate opaque media deeply. Specifically, ultrasound has been widely used in numerous biological and clinical applications.[3,4] Acoustic tweezers have been shown to have great potential in clinical medical applications because they can penetrate deeply, cause less tissue damage, and make no contact with the target. In 1991, Wu generated a stable force potential well in ultrasonic standing waves by applying two opposing transducers and introduced the term acoustic tweezers.[5] To date, two opposing transducers have been used to emit ultrasonic standing waves to aggregate microparticles.[6,7]

Although standing waves have been shown to manipulate particles and even living things,[8,9] the operation is limited to a fixed area between transducers. Glauber T designed single-beam multitrapping acoustical tweezers, which improve the ability to manipulate particles.[10] In addition, with multiple transducers, an acoustic vortex can be formed by controlling the phase of each element in the array.[11] This allows particles to be captured at multiple positions in the axial direction.

In Ref. [12], 64 transducers operating at 2.35 MHz have been designed to form an array to aggregate 90 μm diameter polystyrene particles into a ring. Hong *et al.*[13] demonstrated the ability of a small number of peripherally placed sources to generate acoustic vortex fields and stably levitate a wide range of liquid and solid objects. Fan and Zhang[14] suggested the flexibility of trapping both relatively dense and stiff particles and relatively light and soft particles at the pressure maximum of the axisymmetric Bessel beam in the Rayleigh regime. Therefore, the study of focused ultrasound has more practical significance. The weakly-focused acoustic vortex was generated by applying an elevation angle to the planar transducers of an N-element ring array, enabling large-scale object manipulation.[15] Diego Baresch *et al*. used a spherical transducer to generate high-order focused acoustic vortices (FAVs) and simulated particle motion driven by the acoustic radiation force (ARF).[16] It was discovered that the majority of the energy within the focused sound beam converged in a confined region, creating a distinct focal point. This observation indicates that the concentrated acoustic beam possesses the capability to significantly enhance the efficiency of particle manipulation, with the focal zone positioned in close proximity to the acoustic source. The angular momentum transfer from acoustic vortices causes the particles to rotate around the axis, while the axial component either pushes them away from or towards the acoustic source.[17] A 17.9 MHz meshed transmitter integrates with a Fresnel lens to focus a zero-order Bessel beam. This precision tool can trap particles between 70 μm and 90 μm,[18] even at the axial area between the focal point and the acoustic source.[19] These experiments involve objects much smaller than the wavelength of the acoustic wave, i.e., the Rayleigh particle.

[†]Corresponding author. E-mail: wangqingdong@sdust.edu.cn

© 2025 Chinese Physical Society and IOP Publishing Ltd. All rights, including for text and data mining, AI training, and similar technologies, are reserved.

A sine-driven lithium niobate-focused transducer operating at 30 MHz has been designed to manipulate lipid microdroplets.[20] It has been demonstrated that lipid microdroplets around the focal point can be trapped in the focus center. The force is correlated with the size of the lipid microdroplets, the acoustic frequency, and the excitation energy of the acoustic source, and the size of the trapped particles decreases as the acoustic frequency increases. In the study of ray optics, a Janus particle with a diameter of 2 μm is displaced from the optical axis beam to a new equilibrium position. The simplicity and efficiency of the ray model make it popular in optical and acoustic tweezer particle motion studies due to its less resource consumption and fast calculation.[21]

In the study of the ARF, another significant particle, in addition to the Rayleigh particle,[22] is the Mie particle, which has a diameter much larger than the wavelength. During the study of Mie particles, researchers have found that the magnitude and direction of the ARF experienced by the particles are closely linked to the shape and size of the receiving microspheres. The receptor described in this study is assumed to be spherical, with a diameter equal to the wavelength of the acoustic wave. Experiments have demonstrated that acoustic vortices can trap particles at the position of maximum acoustic pressure and cause them to move in a rotational motion around the vortex center in a ring trajectory.

2. Model

In this study, the propagation of acoustic waves in the acoustic lens is calculated using wave acoustics, while the acoustic field in the water medium is determined through ray acoustics. The combination of both methodologies constitutes a hybrid calculation method that integrates wave and ray acoustics. The wave acoustics calculates regions near the sound source or areas with spatial discontinuities, while the ray acoustics computes large-scale propagation. The computational results align with those obtained using either method independently. Thus, the hybrid approach achieves an optimal balance between efficiency and accuracy.

To determine the acoustic pressure on the surface of the acoustic lens, a numerical simulation model was developed. The acoustic pressure within the acoustic lens is computed numerically using finite element software. By adjusting the initial phase of the transducer's vibration velocity, the acoustic vortex fields with different topological charges (TCs) are obtained. The model involves a close connection between the transducer's surface and the acoustic lens. It is posited that the acoustic wave generated by the transducer runs parallel to the acoustic axis within the acoustic lens, propagating towards the interface between the lens and water. Refraction of the acoustic wave occurs at the interface of the medium. By employing the method of ray acoustics and Snell's law, the refraction angle of the acoustic wave at the interface can be calculated. Each point on the medium interface can be treated as a point source, assuming the presence of a uniform sphere with a refractive index higher than that of liquid water. When an acoustic ray strikes an interface between two media, momentum transfer occurs between them, leading to the ARF.

As shown in Fig. 1, the vector $\boldsymbol{AC}$ is the path from the incident point A to the center of the sphere C, the vector $\boldsymbol{BC}$ is the path from the acoustic source point B to the center of the sphere C, vector $\boldsymbol{BA}$ is the path from the acoustic source point B to the incident point A, $\alpha = \arccos(\frac{\boldsymbol{BA}\cdot\boldsymbol{BC}}{|\boldsymbol{BA}\cdot\boldsymbol{BC}|})$, incident angle $\theta_{\rm i} = \arccos(\frac{\boldsymbol{BA}\cdot\boldsymbol{AC}}{|\boldsymbol{BA}\cdot\boldsymbol{AC}|})$, refraction angle $\theta_{\rm r} = \arcsin(\frac{\sin\theta_{\rm i} n_1}{n_2})$, where n_1 and n_2 are the refractive indices of the medium and the sphere, respectively.

$$Q_{\rm s} = 1 + R\cos 2\theta_{\rm i} - \frac{T^2[\cos(2\theta_{\rm i} - 2\theta_{\rm r}) + R\cos 2\theta_{\rm i}]}{1 + R^2 + 2R\cos 2\theta_{\rm r}}, \tag{1}$$

$$Q_{\rm g} = -R\sin 2\theta_{\rm i} + \frac{T^2[\sin(2\theta_{\rm i} - 2\theta_{\rm r}) + R\sin 2\theta_{\rm i}]}{1 + R^2 + 2R\cos 2\theta_{\rm r}}, \tag{2}$$

$$R = \left|\frac{Z_2/\cos\theta_{\rm r} - Z_1/\cos\theta_{\rm i}}{Z_2/\cos\theta_{\rm r} + Z_1/\cos\theta}\right|^2, \tag{3}$$

$$H(\theta) = \cos\theta_{\rm i}\sin\theta\left\{\cos(\theta_{\rm i} - \theta) + R\cos(\theta_{\rm i} + \theta) - \frac{T^2[\cos(\theta_{\rm i} - 2\theta_{\rm r} + \theta) + R\cos(\theta_{\rm i} + \theta)]}{1 + R^2 + 2R\cos 2\theta_{\rm r}}\right\}, \tag{4}$$

where $Q_{\rm s}$ and $Q_{\rm g}$ represent the scattering force and gradient force coefficients,[23] R is the Fresnel reflection coefficient, and transmission coefficient $T = 1 - R$, Z_1 and Z_2 are the acoustic impedances in the medium and inside the sphere, respectively. $H(\theta)$ represents the fraction of the initial ARF acting on the surface of the sphere.

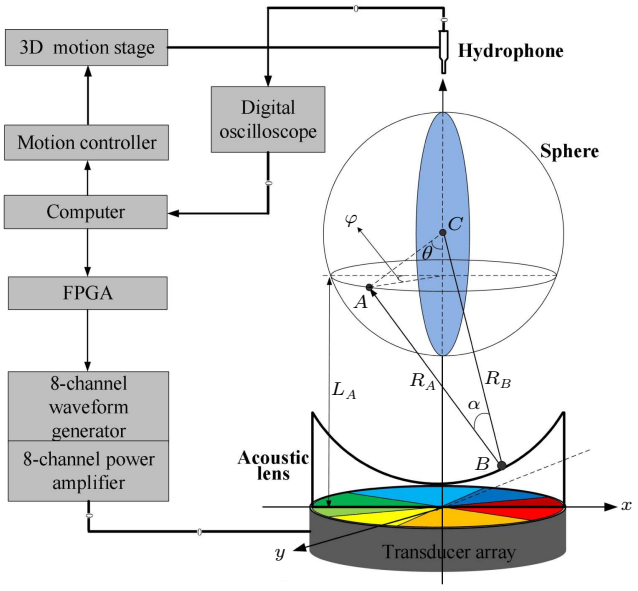


Fig. 1. Schematic diagram of the correlation between the transducer array control process and the sound field calculation model.

The ARF equals the power divided by the acoustic velocity $F = W/L = (P \times t)/(c_w \times t) = P/c_w$.[24] Here, t represents time, W represents the work done by the force, L represents the displacement of the force, P represents power, and c_w represents acoustic speed.

A sphere's surface shows acoustic intensity equivalent to the power at that location. The scattering force and the gradient force formed by the k-th sound ray can be expressed as

$$\boldsymbol{F}_s = Q_s \frac{I_k \Delta S \cos\theta_i}{c_w} \boldsymbol{s} = Q_s \frac{I_k \Delta S \cos\theta_i}{c_w} (s_x, s_y, s_z), \quad (5)$$

$$\boldsymbol{F}_g = Q_g \frac{I_k \Delta S \cos\theta_i}{c_w} \boldsymbol{g} = Q_g \frac{I_k \Delta S \cos\theta_i}{c_w} (g_x, g_y, g_z). \quad (6)$$

Point source B generates three directed forces at point A, shown in these three equations. Among them, ΔS and I_k represent the area and intensity. The unit vector of the scattering component $\boldsymbol{s}$ is perpendicular to the gradient component $\boldsymbol{g}$.

The ARF acting on a sphere caused by all acoustic sources:

$$F_x = F_{xs} + F_{xg} = \sum_{k=1}^{M} \sum_{j=1}^{N} \frac{\Delta S}{c_w} \frac{I_{jk} \cos\theta_i}{R_A} \times \left[\left(Q_s + \frac{Q_g}{\tan\alpha} \right) x_A - \frac{R_A Q_g}{L_B \sin\alpha} x_C \right], \quad (7)$$

$$F_y = F_{ys} + F_{yg} = \sum_{k=1}^{M} \sum_{j=1}^{N} \frac{\Delta S}{c_w} \frac{I_{jk} \cos\theta_i}{R_A} \times \left[\left(Q_s + \frac{Q_g}{\tan\alpha} \right) y_A - \frac{R_A Q_g}{L_B \sin\alpha} y_C \right], \quad (8)$$

$$F_z = F_{zs} + F_{zg} = \sum_{k=1}^{M} \sum_{j=1}^{N} \frac{\Delta S}{c_w} \frac{I_{jk} \cos\theta_i}{R_A} \times \left[\left(Q_s + \frac{Q_g}{\tan\alpha} - \frac{R_A Q_g}{L_B \sin\alpha} x_C \right) L_A - \frac{r R_A Q_g \cos\theta}{L_B \sin\alpha} \right], \quad (9)$$

where M and N represent the number of force-receiving points on the surface of the small sphere and the number of acoustic rays, respectively .

Numerical simulations of FAVs were performed using the MATLAB software. The practical parameters of the experimental system were used to simulate the distributions of the acoustic pressure and the ARF for FAVs of different orders. The circular array consisting of 8 planar sector transducers with radius $a = 40$ mm and a central angle $\Delta\varphi = \pi/4$ was used as the source. The working frequency was set to 500 kHz, and the acoustic speed and density of the water were set to $c_w = 1500$ m/s, $\rho_w = 1000$ kg/m^3. The acoustic lens (curvature radius 46.19 mm, height 30 mm) was manufactured by three-dimensional printing using acrylonitrile butadiene styrene resin, and its parameters were measured as acoustic speed $c_1 = 2146$ m/s, density $\rho_1 = 1023$ kg/m^3, attenuation coefficient $\alpha = 1.8$ dB/cm, and refractive index $\beta = 1.56$.

The ARF acting on a particle in an acoustic field is influenced by various factors, with particle size being one of them. Mie particles and Rayleigh particles exhibit different motion states in the same acoustic field. The radial ARF distribution for spherical particles in a focused acoustic field is illustrated in Fig. 2. With the acoustic field TC $l = 0$, the peak acoustic pressure acts on the center of the cross-section, exerting a force on particles within it. Assume that the center of gravity of the small sphere is at the origin of the *xoy* plane, where the acoustic propagation axis is located. For a particle diameter $D = \lambda$, the radial force component keeps the sphere balanced, firmly adhering it to the sound axis. Any external force that slightly shifts the sphere off this axis will bring it back due to the pull of the acoustic wave. For a particle diameter of $D = 2\lambda$, the force impact remains similar, but its amplitude increases.

Figure 2(b) at $z = 130$ mm illustrates the radial ARF. For particles with diameters of 1λ and 4λ, the acoustic propagation axis represents the equilibrium position. Around $x = 0$, the direction of force is the same as that of displacement and the force increases rapidly, making it prone to move away from the acoustic axis. Therefore, not all particles larger than the wavelength can be aggregated to the acoustic axis. As the particle diameter increases, the ARF it receives also increases. Compared with Fig. 2(a), the radial ARF varies at different axial positions.

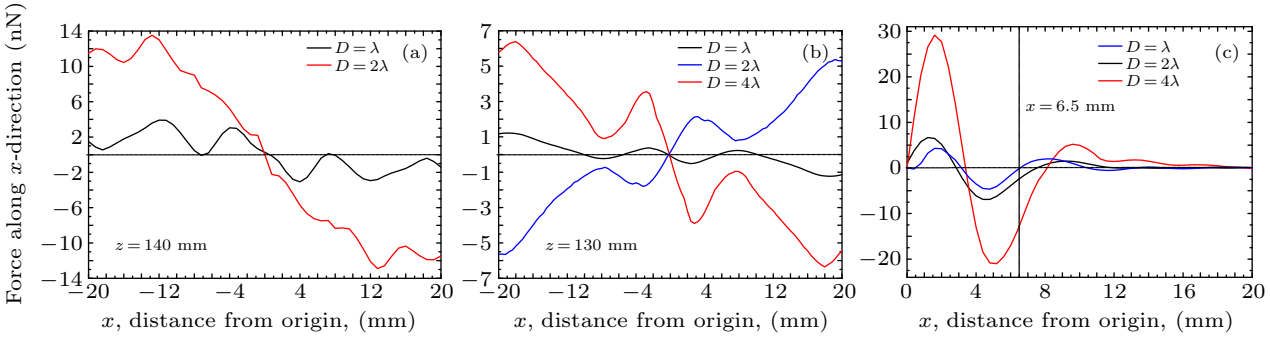


Fig. 2. Distribution of radial ARFs at axial positions (a) $z = 140$ mm and (b) $z = 130$ mm in a focused acoustic field with a TC of $l = 0$. (c) For TC $l = 2$, the distribution of radial ARF received by spheres with the diameter $D = \lambda, 2\lambda, 4\lambda$.

In an acoustic vortex field with non-zero integer TC, acoustic waves form a spiral pattern, generating a central acoustic vortex and a high-intensity point at its radius. The vortex's central well potential and orbital angular momentum trap Rayleigh particles, causing them to rotate. For TC $l = 2$, there exists an additional balancing point beyond the vortex radius where a particle with a diameter $D = \lambda$ can achieve radial equilibrium at a certain radial distance $r = 6.5$ mm, creating an annular equilibrium zone as shown in Fig. 2(c). The orbital angular momentum from the vortex is transferred to the particle, causing it to spin around the vortex center. As the particle's radius increases, the equilibrium position's radius also increases. For example, particles with diameters 2λ and 4λ have radial equilibrium positions at 7.6 mm and 8.4 mm, respectively. This increase in size leads to a corresponding increase in the ARF experienced by the particle.

3. Experimental studies

Figure 1 illustrates our experimental setup, which includes a sector planar piston transducer array, an acoustic lens, and an acoustic source driver signal control system. The acoustic source array that comprises 8 sector transducers is centered. The acoustic source driver signal control system consists of an FPGA, an 8-channel MD2134 unit module, and an amplification module. In the experiment, each transducer is driven by a continuous sine signal with a frequency of 500 kHz. A 1 mm needle hydrophone is used to collect the acoustic pressure signal, with a step of 0.8 mm each time. A controlled polyethylene sphere floats at the interface of water and air, and its movement is recorded by the camera. Other parameters in the experiment are consistent with those used in the simulation.

The cross-sectional distributions of the acoustic pressure are illustrated in Fig. 3. At an axial distance of 130 mm, (a), (b), and (c) depict simulated pressure maps for $l = 1$, 2, and 3, respectively. The lens efficiently focuses energy into the paraxial region of the vortex where the central pressure is zero. As the TC increases, the vortex radius expands, the range of trapped particles widens, and the acoustic pressure at the vortex radius decreases. For $l = 2$, the peak radial acoustic pressure occurs at $x = 6.5$ mm, or the vortex radius. The experimental acoustic pressure distributions obtained are shown in Figs. 3(d)–3(f), with TCs of $l = 1$, $l = 2$, and $l = 3$, respectively. The outcomes obtained are in remarkable agreement with the simulation results, exhibiting a high degree of consistency.

Figure 4 illustrates the sphere's motion in an acoustic field with $l = 0$. The sphere, measuring 1.5 mm in radius and made of polyethylene, is positioned at $z = 130$ mm. The red dot is the center of the cross-section of this acoustic field, while the green dot represents the geometric center of the sphere. First, the sphere is securely held at the origin by the focused acoustic field, aligning its center with the origin in Fig. 4(a). Since $l = 0$, the sphere remains stationary as there is no orbital angular momentum. Second, the transducers are turned off to release the particle, then the sphere moves slightly away from the origin ($\Delta s = 0.8$ mm) as shown in Fig. 4(b). When the transducers are turned on, they promptly pull the sphere back to its original position. Third, the acoustic field displaces the sphere further by $\Delta s' = 2$ mm in Fig. 4(c). When the transducers are activated, the sphere moves away from the origin. This indicates that when the geometric center of the sphere is at a certain distance from the origin, the focused acoustic field loses its ability to capture the sphere.

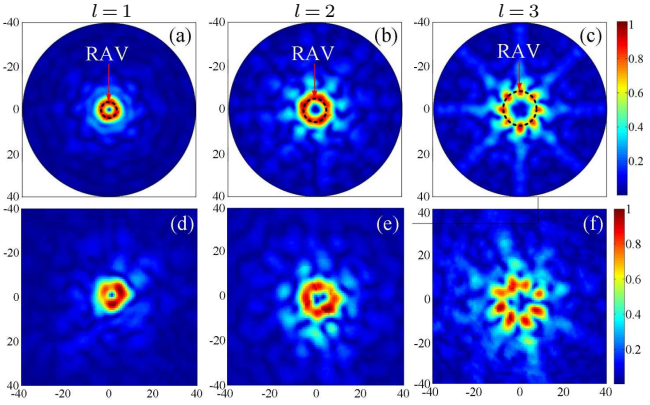


Fig. 3. Cross-sectional simulation (a)–(c) and experiments (d)–(f) of the focused acoustic vortex acoustic pressure distribution, axial distance of $z = 130$ mm, with topological charges of $l = 1$–3, respectively.

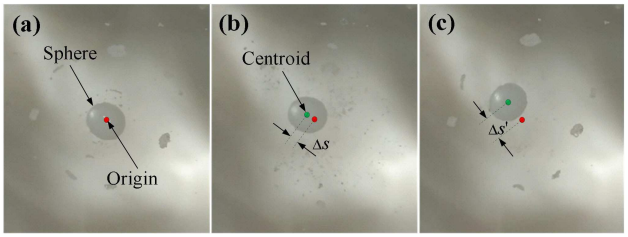


Fig. 4. The TC $l = 0$ of the focused acoustic field and the corresponding position of the particle when the acoustic source is on (a) and off (b), (c).

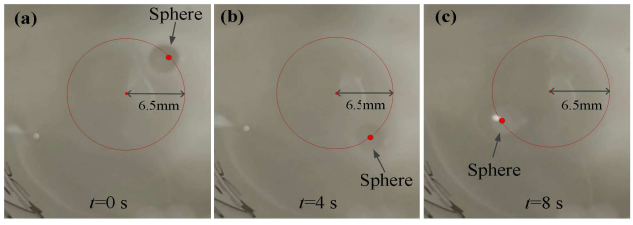


Fig. 5. TC $l = 2$ of the focusing vortex acoustic field, the sphere rotates around the focusing region; (a), (b) and (c) show the positions of the sphere at different times.

The vortex center can form acoustic traps to trap and rotate the sphere. The region outside the vortex center can also form a trapped annulus. Once the acoustic field of the FAV traps the sphere at the maximum annular acoustic pressure, the sphere will rotate around the vortex center along the annular trajectory due to the orbital angular momentum. The

experiment employs a sphere with a diameter $D = \lambda$ and a TC $l = 2$. It forms a circular orbit around the vortex center at 6.5 mm, which is consistent with the trapping position revealed in Fig. 2(c). The positions of the sphere at $t = 0$ s, 4 s, and 8 s are shown in Figs. 5(a)–5(c). It takes approximately 17 s for the sphere to complete one full rotation around the ring. In this study, the viscous force generated by particle motion manifests as a resistance force, expressed as $F_D = -3\pi\mu DV$, where μ is the dynamic viscosity of the fluid, and $V = u_\mathrm{f} - u_\mathrm{p}$ is the relative velocity between the particle and fluid. Due to the relatively large particle size, the viscous force constitutes a non-dominant factor in particle motion.

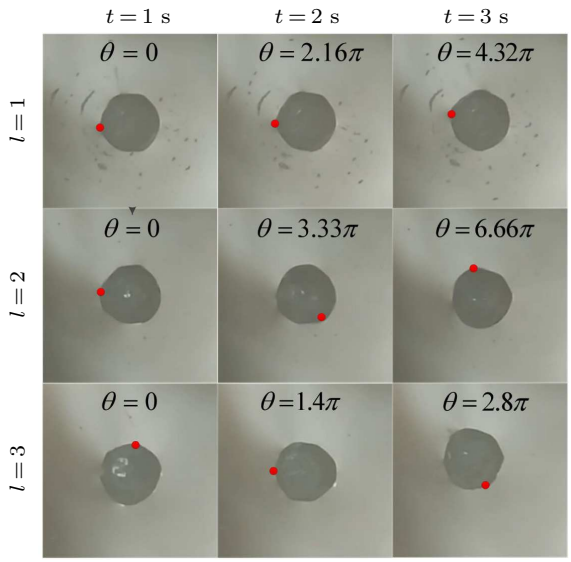


Fig. 6. The sphere rotates in the vortex center of the FAVs with TCs of (first row) $l = 1$, (second row) $l = 2$, and (third row) $l = 3$. The first, second, and third columns represent the positions of the spheres at time $t = 1$ s, 2 s, and 3 s, respectively.

The sector transducer array and acoustic lens create a field of FAV with zero pressure at the center of the vortex. This field possesses orbital angular momentum, causing the sphere not only to be trapped at the center of the potential well position but also to rotate within the vortex. After determining the diameter of the sphere and the axial position of its vortex acoustic field, the sphere rotates at various speeds corresponding to different TCs. It is well known that the larger the TC, the larger the vortex radius, meaning the distance of the peak acoustic pressure from the geometrical center of the sphere increases. However, when the diameter of the sphere is much smaller than the vortex radius, the rotational speed is almost independent of the size of the TC. When the diameter of the sphere is comparable to the vortex radius, the rotational speed of the sphere is significantly influenced by its size. The rotational speeds of the blob in the acoustic field with a TC of $l = 1$ (first row), $l = 2$ (second row), and $l = 3$ (third row) are 1.08 r/s, 1.67 r/s, and 0.7 r/s (revolutions per second), respectively, as shown in Fig. 6. The diameter of the blob is approximately 3 mm. The red dot is the new position of a point on the blob after a certain rotation angle, and the value of θ in the figure indicates the angle of rotation of the red dot. It can be observed that the rotational speed of the blob does not increase with an increase in the TC. The fastest rotational speed of the blob occurs at the TC $l = 2$, which is 1.55 and 2.39 times higher than that at $l = 1$ and $l = 3$, respectively.

4. Conclusion

The manipulation characteristics of large particles by FAVs composed of sector transducer arrays and acoustic lenses are analyzed. A hybrid method that combines the wave equation and ray acoustics is used to calculate the acoustic field. The two-dimensional distribution of acoustic pressure in the acoustic field is obtained through simulation. The acoustic pressure distributions from numerical simulation and experimental measurements show good agreement. In the vortex acoustic field, it has been demonstrated for the first time that particles with a diameter equal to the wavelength will move in circular trajectories, rotating along an annular orbit once they are trapped at the vortex radius.

Acoustic lenses enhance energy concentration, thereby improving the system's energy efficiency. This study demonstrates, through simulations and experiments, that focused acoustic fields with $l = 0$ provide superior energy concentration by aligning Mie particles with the center of the cross-section. In contrast, the FAVs with $l = 2$, which cannot concentrate energy effectively, create a high-pressure annulus that transfers orbital angular momentum to Mie particles, causing them to move around the annulus. This study advances the research on ultrasonic vortex manipulation of large particles by proposing a cost-effective and biocompatible method. The approach demonstrates the potential for clinical adjuvant therapy applications.

Acknowledgment

Project supported by the National Key R&D Program of China (Grant No. 2023YFE0201900).

References

[1] Ashkin A, Dziedzic J M, Bjorkholm J E and Chu S 1986 *Opt. Lett.* **11** 288
[2] Ashkin A 1997 *Proc. Natl. Acad. Sci. USA* **94** 4853
[3] Lin S C, Mao X and Huang T J 2012 *Lab Chip* **12** 2766
[4] Li Y, Lee C, Chen R, Zhou Q and Shung K K 2014 *Appl. Phys. Lett.* **105** 173701
[5] Wu J R 1991 *J. Acoust. Soc. Am.* **89** 2140
[6] Hertz H M J 1995 *J. Appl. Phys.* **78** 4845
[7] Courtney C R P, Ong C K, Drinkwater B W, Wilcox P D, Demore C, Cochran S, Glynne-Jones P and Hill M 2010 *J. Acoust. Soc. Am.* **128** 195
[8] Meng L, Cai F Y, Chen J J, Niu L L, Li Y M and Wu J R 2012 *Appl. Phys. Lett.* **100** 173701
[9] Bernassau A L, Glynne-Jones P, Gesellchen F, Riehle M and Cumming D R S 2014 *Ultrasonics* **54** 268

[10] Silva G T and Baggio A L 2015 *Ultrasonics* **56** 449
[11] Wang Q D, Li Y Z, Ma Q Y, Guo G P, Tu J and Zhang D 2018 *J. Appl. Phys.* **123** 034901
[12] Courtney C R P, Demore C E M, Wu H, Grinenko A, Wilcox P D, Cochran S and Drinkwater B W 2014 *Appl. Phys. Lett.* **104** 154103
[13] Hong Z Y, Yin J F, Zhai W, Yan N and Drinkwater B W 2017 *Sci. Rep.* **7** 7093
[14] Fan X D and Zhang L 2019 *Phys. Rev. Appl.* **11** 014055
[15] Li Y Z, Li P X, Ding N, Guo G P, Ma Q Y, Tu J and Zhang D 2021 *Chin. Phys. B* **30** 044302
[16] Baresch D, Thomas J L and Marchiano R 2013 *J. Appl. Phys.* **113** 184901
[17] Baresch D, Thomas J L and Marchiano R 2013 *J. Acoust. Soc. Am.* **133** 25
[18] Choe Y, Kim J W, Shung K K and Kim E S 2011 *Appl. Phys. Lett.* **99** 233704
[19] Zhuang H F, Zhang Q Y, Hu G H, Wang Q D and Du L B 2024 *Chin. Phys. B* **33** 074302
[20] Lee J 2009 *Appl. Phys. Lett.* **95** 073701
[21] Liu J, Zhang C, Zong Y W, Guo H L and Li Z Y 2015 *Photon. Res.* **3** 265
[22] Yoo J, Kim J, Lee J and Kim H H 2023 *iScience* **26** 108178
[23] Lee J 2014 *Ultrasonics* **54** 11
[24] Lee J, Ha K and Shung K K 2005 *J. Acoust. Soc. Am.* **117** 3273